Imaging of pH distribution inside individual microdroplet by stimulated Raman microscopy

Kedong Gong[a,b,c,d,1] (iD), Jianpeng Ao[e,f,1] (iD), Kejian Li[a,b,c,d], Le Liu[g], Yangyang Liu[a,b,c,d] (iD), Guanjun Xu[a,b,c,d], Tao Wang[a,b,c,d], Hanyun Cheng[a,b,c], Zimeng Wang[a,b,c,d], Xiuhui Zhang[h] (iD), Haoran Wei[i], Christian George[j] (iD), Abdelwahid Mellouki[k,l] (iD), Hartmut Herrmann[m] (iD), Lin Wang[a,b,c] (iD), Jianmin Chen[a,b,c] (iD), Minbiao Ji[e,f,2] (iD), Liwu Zhang[a,b,c,d,2] (iD), and Joseph S. Francisco[n,o,2] (iD)

Aerosol microdroplets as microreactors for many important atmospheric reactions are ubiquitous in the atmosphere. pH largely regulates the chemical processes within them; however, how pH and chemical species spatially distribute within an atmospheric microdroplet is still under intense debate. The challenge is to measure pH distribution within a tiny volume without affecting the chemical species distribution. We demonstrate a method based on stimulated Raman scattering microscopy to visualize the three-dimensional pH distribution inside single microdroplets of varying sizes. We find that the surface of all microdroplets is more acidic, and a monotonic trend of pH decreasing is observed in the 2.9-μm aerosol microdroplet from center to edge, which is well supported by molecular dynamics simulation. However, bigger cloud microdroplet differs from small aerosol for pH distribution. This size-dependent pH distribution in microdroplets can be related to the surface-to-volume ratio. This work presents noncontact measurement and chemical imaging of pH distribution in microdroplets, filling the gap in our understanding of spatial pH in atmospheric aerosol.

pH distribution | microdroplet | aerosol | stimulated Raman | imaging

Aerosol microdroplets are ubiquitous in the atmosphere; they act as important microreactors for atmospheric reactions (1–3). At local or even global scales, the composition and optical characteristics of these atmospheric microdroplets influence climate change and hence extreme weather by absorbing and scattering solar radiation (1, 4). Benefiting from a large surface-to-volume ratio (S/V) (5, 6), a microdroplet exhibits a large air–water interface which provides a special and unique reaction environment with qualitatively different thermodynamic and kinetic properties compared to bulk solutions (7–9), initiating an acceleration of reactions (10–12), interfacial catalysis, and spontaneous sulfur redox chemistry on the surface of atmospheric microdroplets (13–15).

pH, as one of the most basic chemical parameters, plays an important role in dictating atmospheric process and human health by driving surface tension, phase separation, and gas-particle partitioning of atmospheric microdroplets in numerous ways (6, 16). In general, the average pH of the condensed phase of aerosols, such as that of cloud droplets, could be estimated by thermodynamic models (e.g., E-AIM, ISORROPIA) based on Gibbs free energy minimization or chemical potential methods (16). Nevertheless, the developments of aerosol "chemical mixing state" have proved the importance of the properties of the individual particles for the estimation accuracy of global climate models and understanding the climate and health effects of condensed phases (4, 17). Unfortunately, the absence of a direct pH probe significantly hinders the full understanding of the controls exerted by pH on atmospheric chemistry (17, 18). Micro-Raman spectroscopy (MRS), molecular probes, and optical tweezers have been developed to directly measure the whole pH of the atmospheric microdroplets, but they all worked under the assumption of homogeneous intradroplet acidity and lack spatial resolution (5, 19, 20). Although the nanoprobe assisted by surface-enhanced Raman scattering possesses spatial resolutions, the contacting detection and the uneven distribution of the nanoprobe are hard to be ignored (21).

Up to now, lacking accurate methods, how pH and chemical species spatially distribute within an individual condensed phase has been a subject of intense debate for many years. To solve this puzzle, we developed a noncontact method to measure and visualize pH based on stimulated Raman scattering (SRS) microscopy and studied the pH inside the sulfate-containing microdroplet on a substrate to obtain the spatial distribution of pH inside the single microdroplets, because the acid–conjugate base provides key information about the pH of a system. As a fast-growing technology, SRS enhances the conventional weak Raman scattering by coherent and nonlinear optical process (~10^3 to 10^8 gain) (Fig. 1A), enabling rapid and label-free chemical imaging with intrinsic three-dimensional (3D) sectioning capabilities (22–24). The accurate quantitative analysis and spatial high

Significance

pH plays an important role in chemical reactions related to atmospheric microdroplets. However, the characterization of pH distributions within microdroplets is challenging, and they are often omitted in chemical kinetics models. Through the developed method based on stimulated Raman scattering microscopy, we showed that H$^+$within smaller microdroplets possesses greater preference toward the interface than within larger ones, which generated a spatial pH distribution, implying enhanced interfacial acid catalysis of aerosol microdroplets. The difference in pH distribution trends between small aerosols and bigger cloud microdroplets underscores the crucial role of microdroplet size. These conclusions underscore the overlook of pH spatial distribution and size dependence may lead to discrepancies between model simulation and field measurement.

[1]K.G. and J.A. contributed equally to this work.

[2]To whom correspondence may be addressed. Email: minbiaoj@fudan.edu.cn, zhanglw@fudan.edu.cn, or frjoseph@sas.upenn.edu.

resolution (*SI Appendix*, Note S1) of SRS enabled us to directly detect variations of trace chemicals in microdroplets.

Results

Obtaining Microdroplet pH via SRS. As the dominant inorganic pair of an acid–conjugate base in ambient aerosols, sulfate (SO_4^{2-}) and bisulfate (HSO_4^-) have distinguishable vibrational shifts for $\nu_s(SO_4^{2-})$ and $\nu_s(HSO_4^-)$ at ~985 and ~1,050 cm^{-1}, respectively (Fig. 1*B*). We first measured the SRS spectra of Na$_2$SO$_4$ and NaHSO$_4$ in standard bulk buffer solutions to establish calibration curves of $[SO_4^{2-}]$ and $[HSO_4^-]$ (*SI Appendix*, Fig. S1). As expected, the intensity of $\nu_s(SO_4^{2-})$ and $\nu_s(HSO_4^-)$ increased with concentration (Fig. 1*B*), with a good linear correlation (*SI Appendix*, Fig. S2). Meanwhile, the intensity of $\nu(H_2O)$ (3,420 cm^{-1}) maintains relatively stable (Fig. 1*C*). Geometric factors of microdroplets and the wave nature of light are the major factors that hinder the data interpretation (25); hence, the internal standards (IS) are adapted to correct these possible influences (*SI Appendix*, Note S2). The intensity ratio of ν_s $(SO_4^{2-})/\nu(H_2O)$ and $\nu_s(HSO_4^-)/\nu(H_2O)$ exhibits an excellent linear relationship with the $[SO_4^{2-}]$ and $[HSO_4^-]$ ($R^2 = 1.000$ and 0.994, Fig. 1*D*), which allows the quantification of $[SO_4^{2-}]$ and $[HSO_4^-]$. We also showcased the reliability of this linear fit by repeating this IS method with the MRS (13, 25, 26) (*SI Appendix*, Figs. S3 and S4). Although the detected $[SO_4^{2-}]_{MRS}$ and $[HSO_4^-]_{MRS}$

through MRS are similar to those of SRS (Fig. 1*E*), the latter exhibits significantly higher precision due to a stable calibration curve (detailed in *SI Appendix*, Note S3). The sum of the detected $[SO_4^{2-}]_{SRS}$ and $[HSO_4^-]_{SRS}$ of a series of mixed solutions is almost equal to the preknown total [S] with a *P*-value of 0.941. These consistencies solidify the potential of SRS for pH detection by high discrimination for the dissociation of SO_4^{2-}/HSO_4^-.

To elucidate the pH distribution within whole microdroplet aerosol, we have derived an analytical expression for pH calculation with $[SO_4^{2-}]$ and $[HSO_4^-]$ based on the definition of acidity and Debye–Hückel theory (27), as detailed in *SI Appendix*, Note S4.

$$pH = pK_a - \log\left(\frac{[HSO_4^-]}{[SO_4^{2-}]}\right) - \log\left(\frac{\gamma_{HSO_4^-}}{\gamma_{SO_4^{2-}}}\right) \quad [1A]$$

The pK$_a$ is the dissociation constant of HSO_4^-, considered as a fixed value (a reasonable explanation is provided in *SI Appendix*, Note S5). Log($\gamma_{bisulfate}/\gamma_{sulfate}$), a derived term, may represent the effect of ionic strength on the activity coefficient. Physically, the activity coefficient of ions comes from the effect of interionic forces and ion-solvent molecular forces on the free energy of ions in solution (28). As shown in Fig. 1*F*, log($\gamma_{bisulfate}/\gamma_{sulfate}$) exhibits an obvious linear relationship with $\sqrt{4 \times [SO_4^{2-}] + [HSO_4^-]}$ that

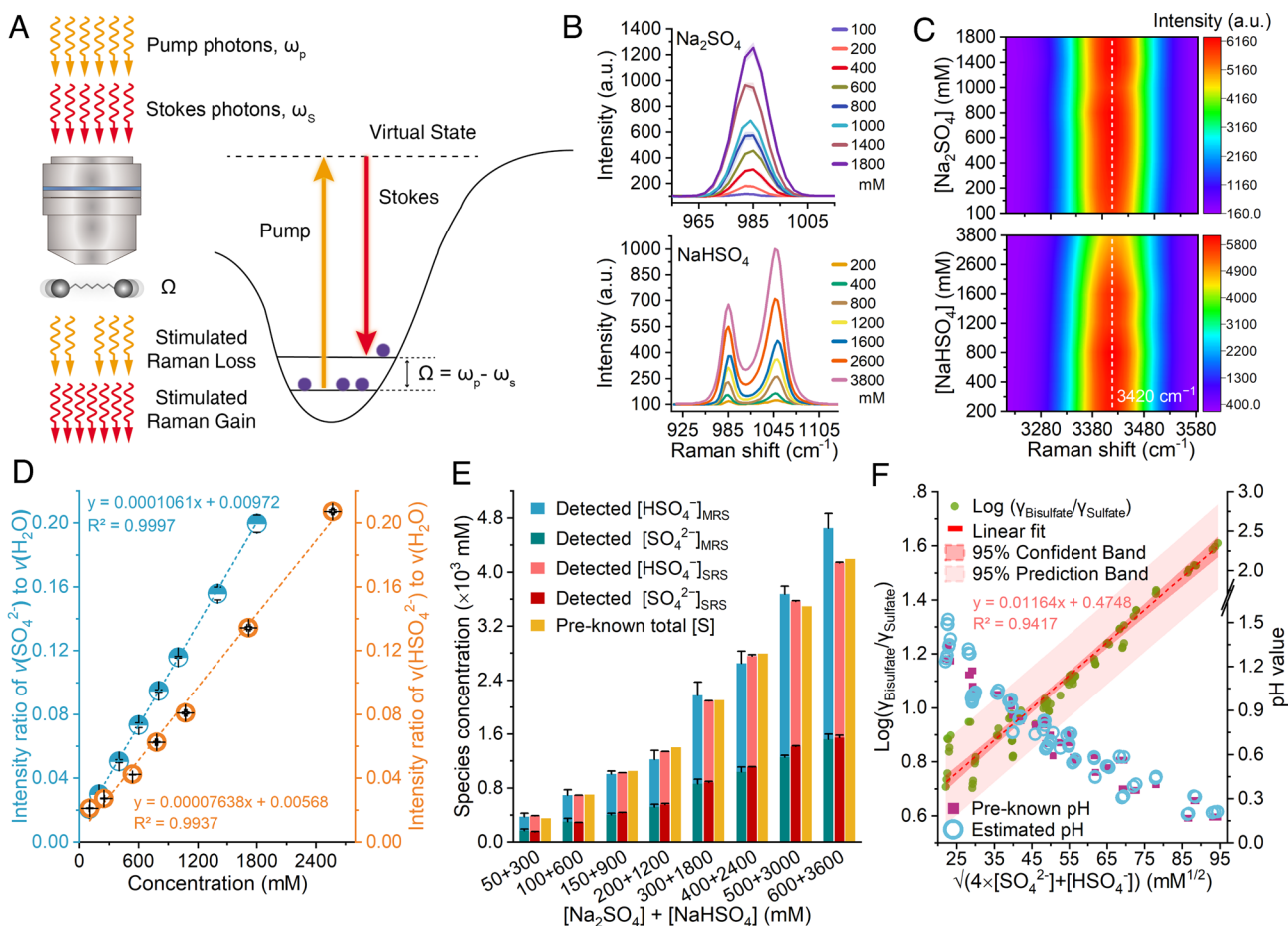**Fig. 1.** Calibration of $[SO_4^{2-}]$ and $[HSO_4^-]$ with pH via SRS. (*A*) The principle of SRS microscopy. (*B*) The SRS spectra of sulfates in standard solutions of Na$_2$SO$_4$ (955 to 1,015 cm^{-1}) and NaHSO$_4$ (910 to 1,130 cm^{-1}). (*C*) The SRS spectra of H$_2$O in the above Na$_2$SO$_4$ and NaHSO$_4$ solutions range from 3,214 to 3,584 cm^{-1}. (*D*) SRS intensity ratio of $\nu_s(SO_4^{2-})/\nu(H_2O)$ and $\nu_s(HSO_4^-)/\nu(H_2O)$ as a function of the $[SO_4^{2-}]$ and $[HSO_4^-]$. (*E*) Comparison of measured $[SO_4^{2-}]$ and $[HSO_4^-]$ by SRS and MRS. They were marked as $[SO_4^{2-}]_{SRS}$, $[HSO_4^-]_{SRS}$, $[SO_4^{2-}]_{MRS}$, and $[HSO_4^-]_{MRS}$, respectively. (*F*) Dependence of the Log$\left(\frac{\gamma_{SO_4^{2-}}}{\gamma_{HSO_4^-}}\right)$ and pH on $\sqrt{4 \times [SO_4^{2-}] + [HSO_4^-]}$. The log($\gamma_{bisulfate}/\gamma_{sulfate}$) was solved using Eq. **1**A and premeasured pH from a probe, and the estimated pH was calculated via Eqs. **1A** and **1B** and SRS spectra.

derived from the ionic strength formula. Then, $\log(\gamma_{bisulfate}/\gamma_{sulfate})$ can be obtained via Eq. **1B**.

$$\log\left(\frac{\gamma_{HSO_4^-}}{\gamma_{SO_4^{2-}}}\right) = a \cdot \sqrt{4 \times [SO_4^{2-}] + [HSO_4^-]} - b \quad [\mathbf{1B}]$$

where a and b, the constants of the calibration curve, were determined at 0.01164 and 0.4748 by the linear fitting (Fig. 1F), respectively, wherein the $\log(\gamma_{bisulfate}/\gamma_{sulfate})$ was solved with Eq. **1A** and preknown pH of NaHSO₄ standard solutions and mixed solutions. Despite slight fluctuations, the difference between the estimated pH (via Eqs. **1A** and **1B**) and preknown pH in Fig. 1F is insignificant ($P = 0.976$, one-tailed t test). Meanwhile, the P-value of estimated pH via MRS and preknown pH is 0.054 (*SI Appendix*, Fig. S5), indicating the accuracy of SRS and versatility of Eqs. **1A** and **1B**. Notably, the regressive Eq. **1B** cannot cover the high-concentration cases within the supersaturated aerosol, but the thermodynamic model evaluation demonstrated the practicability of Eq. **1**B for estimating the pH of microdroplet with high $\log(\gamma_{bisulfate}/\gamma_{sulfate})$ (*SI Appendix*, Note S5 and Figs. S6 and S7).

Monotonic pH Variation inside Small Aerosol Microdroplet. Aerosol microdroplet with a diameter of 2.9 µm was characterized to explore the possible two-dimensional (2D) pH distribution within their bulk under a steady-state environment based on a superhydrophobic substrate (*SI Appendix*, Note S6 and Figs. S8 and S9 and Movie S1). Fig. 2A shows SRS images that track the Raman intensities of $\nu(H_2O)$, $\nu_s(SO_4^{2-})$, and $\nu_s(HSO_4^-)$ of a ~2.9-µm microdroplet. The SRS image of $\nu(H_2O)$ demonstrated a higher intensity in the centroid region, which decreased as the objective moved to the microdroplet edge owing to the reduced actual volume that was probed by SRS. Unexpectedly, the intensities of both $\nu_s(SO_4^{2-})$ and $\nu_s(HSO_4^-)$ were higher at the microdroplet edge. Fig. 2B plotted the distributions of $[SO_4^{2-}]$, $[HSO_4^-]$, as well as pH within a microdroplet. Evidently, all these substances including $[H^+]$ (10^{-pH}) exhibited a strong tendency of interfacial enrichment, with
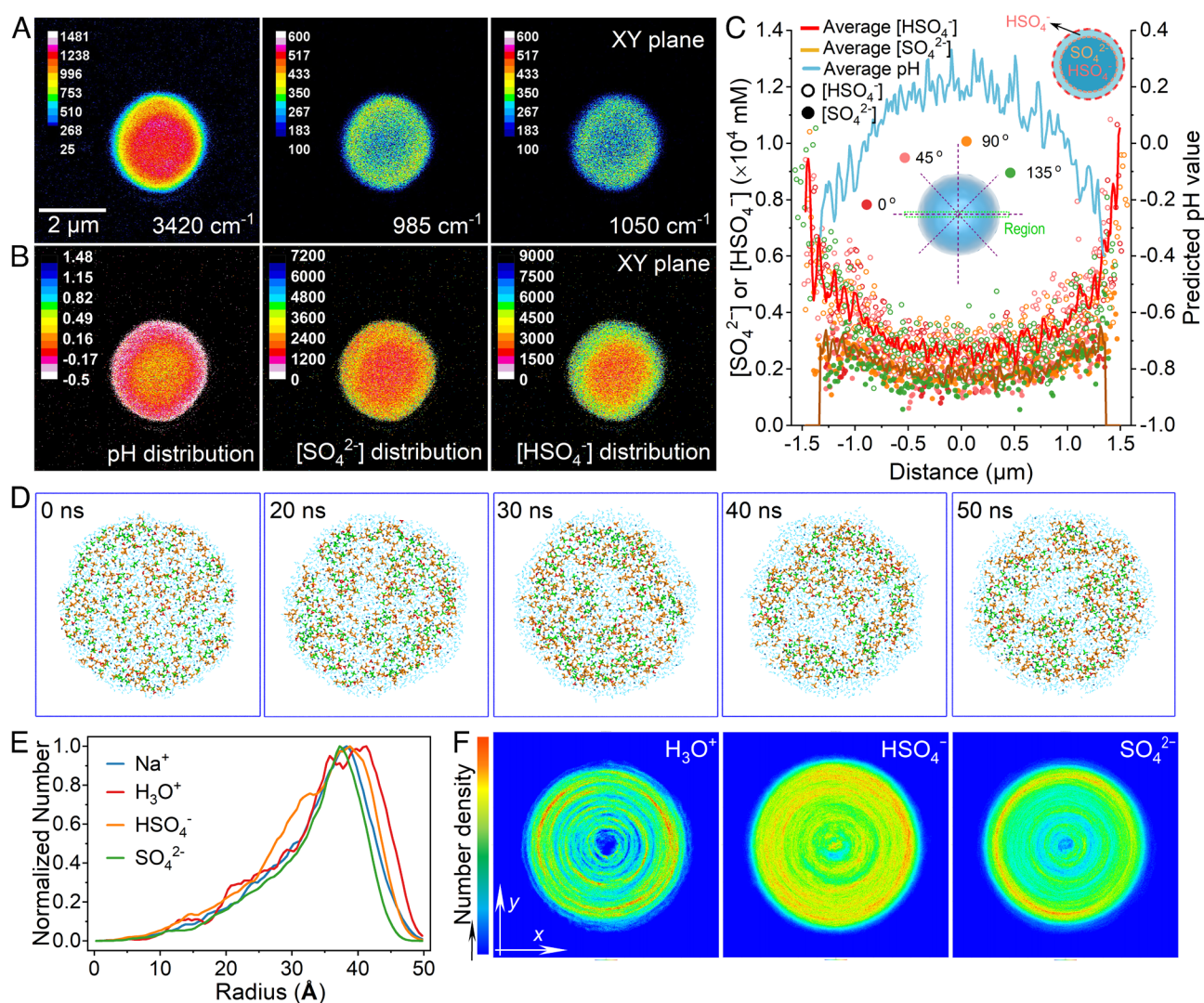

Fig. 2. Stereoscopic pH distribution inside small aerosol microdroplet. (A–C) 2D distribution of SO_4^{2-}, HSO_4^-, and pH in XY plane of the microdroplet (d = ~2.9 µm). (A) SRS images of microdroplet at the Raman shifts of 3,420 cm⁻¹ (H₂O), 985 cm⁻¹ (SO_4^{2-}), and 1,050 cm⁻¹ (HSO_4^-). (B) The chemical imaging of pH, $[SO_4^{2-}]$, and $[HSO_4^-]$ within microdroplet. (C) The $[SO_4^{2-}]$, $[HSO_4^-]$, and pH inside microdroplet as a function of distance to central. The $[SO_4^{2-}]$ and $[HSO_4^-]$ calculated from four single line profiles (0°, 45°, 90°, and 135°) marked as circular scatters while the average $[SO_4^{2-}]$, $[HSO_4^-]$, and pH calculated from parallel line profiles (green box) marked as lines. Inset shows the diagram of the line profile and distribution zone of (bi)sulfates. (D and E) Molecular dynamics of nanodroplet. (D) Snapshots of a sulfate water nanodroplet (5 nm) vs. time. Sticks in red, orange, green, dark blue, and light blue represent H₃O⁺, HSO₄⁻, SO₄²⁻, Na⁺, and water molecules, respectively ($[HSO_4^-] = 3.8$ M, $[SO_4^{2-}] = 2.3$ M, $[H^+] = 1.047$ M). (E) Number profiles of molecules from classical MD trajectories of the water nanodroplet along the radial direction. (F) Projections along Z of coarse-grained simulation data showing the number density distribution of H₃O⁺, HSO₄⁻, and SO₄²⁻ within nanodroplet.

a sharp increase of concentrations from the microdroplet center to the edge. This concentration gradient within a microdroplet was confirmed by MRS as well (*SI Appendix*, Fig. S10), despite the lower spatial resolution. Similarly, for bulk solutions, the species at the air–water interface also represented enrichment (*SI Appendix*, Fig. S11), consistent with the trend observed in microdroplets. The concentration gradient of $[SO_4^{2-}]$ diminished as the probe laser moved deep into the bulk phase of the solution (*SI Appendix*, Fig. S12).

The distributions of $[SO_4^{2-}]$, $[HSO_4^-]$, and pH within a 2.9-μm microdroplet were detailed via the line profile and its representative average (*SI Appendix*, Note S7 and Fig. S13). As shown in Fig. 2C, the distributions of $[SO_4^{2-}]$ and $[HSO_4^-]$ derived from four line profiles (marked by purple dashed lines in the inset) exhibited very similar trends, implying that these distributions are centrosymmetric. Specifically, the $[SO_4^{2-}]$ increased from 1803.5 to 3306.2 mM (1.8-fold increase) as the probe laser moved 1.3-μm away from the microdroplet center, and then cannot be detected when the probe moved further away. Meanwhile, $[HSO_4^-]$ increased from 2746.6 to 9443.8 mM (3.4-fold increase) from 0.0 (center) to 1.5 μm (edge), indicating a stronger interfacial enrichment (Fig. 2 C, *Inset*). In contrast to the strong enrichment of HSO_4^- at the interface, $[SO_4^{2-}]$ may be rapidly reduced below the detection limit of SRS due to the rapid conversion of SO_4^{2-} to HSO_4^- under low pH (<–0.41). Based on the distributions of $[SO_4^{2-}]$ and $[HSO_4^-]$, we found that the pH within the 2.9-μm microdroplet gradually decreased from center to edge. The pH (–0.34) at the microdroplet edge is much more acidic than the centroid (0.19), with $[H^+]$ increased to 2.19 M at the edge (3.4-fold compared with the centroid).

This pH distribution was further examined through classical molecular dynamics (MD) simulations (29). Fig. 2D depicts the time-dependent snapshots of H_3O^+, HSO_4^-, Na^+, and SO_4^{2-} in a water nanodroplet (10 nm) from 0 to 50 ns. These species migrate toward the droplet edge, achieving a relatively stable distribution after 40 ns. Fig. 2E shows the total number profiles of these species along the radius direction (from center to edge) at 50 ns. Species number within the nanodroplet obviously increased from center to edge, which is in accordance with the experimental results

(Fig. 2 A–C). Besides, the number density distribution of H_3O^+, HSO_4^-, and SO_4^{2-} within a nanodroplet (Fig. 2F) is comparable with the chemical imaging results of a small microdroplet (Fig. 2B). Here, simulated H_3O^+ ions have a relatively greater propensity for the air–water interface compared with other ions, supporting the experimental results of the detected pH distribution in the aerosol microdroplets.

Nonmonotonic pH Variation inside Bigger Cloud Microdroplet. Further, the 3D chemical distribution of a bigger microdroplet (27.0 μm) with a lower sulfates concentration was reconstructed (Movie S2) to explore the pH distribution within atmospheric cloud microdroplets. Fig. 3A shows its 2D pH distribution at different Z values (SO_4^{2-} or HSO_4^- distribution is in *SI Appendix*, Fig. S14). The distribution of pH and (bi)sulfate at different Z-values is central symmetric, with lower pH at edges in any direction compared with the microdroplet center. Meanwhile, Fig. 3B shows that the pH distribution in the XZ plane is axisymmetric and similar to the one in the XY plane at Z = 0.0 μm (white box in Fig. 2D). These results demonstrated a central symmetric pH distribution within the entire volume of cloud microdroplets.

The Fig. 3C details this pH distribution where pH remains stable (~0.27) within the distance of 9.5 μm from the center, and down to a pH value of ~ –0.09 at the edge. The difference (0.69 M) in $[H^+]$ between the center and edge here is much smaller than that (1.54 M) for a 2.9-μm microdroplet, indicating that the particle size plays a key role in the H^+ enrichment at the interface. Interestingly, this process of pH decreasing from center to edge is not always monotonous. There is an unexpected pH increase at the inner layer near the edge of the 27.0-μm microdroplet, which is not observed in the case of the 2.9-μm microdroplet. In detail, from the center toward the microdroplet edge, along X, Y, and Z directions, pH first increases from 0.27 to 0.35, then sharply decreases to –0.09 at the interface. Fig. 3D shows the constructed model of 3D pH distribution in small aerosol and big cloud microdroplets based on the aqueous microdroplets with sizes of 2.9 and 27.0 μm, respectively. The notable difference is that cloud microdroplets possess a nonmonotonic pH variation and an abnormal increase in pH
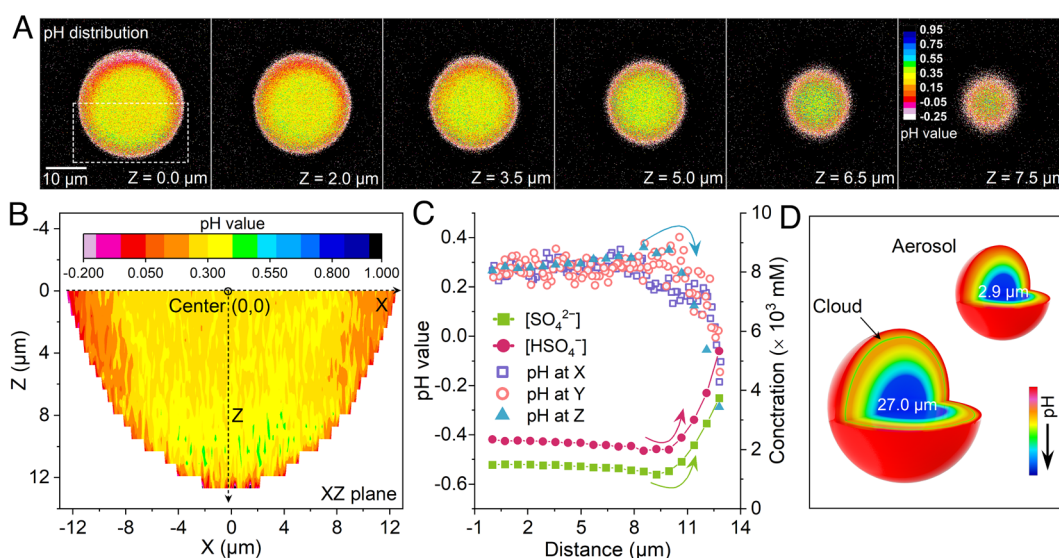

Fig. 3. Stereoscopic pH distribution inside bigger cloud microdroplet. (*A*) pH distribution in XY plane of the 27.0-μm microdroplet with different z values (droplet center is set as 0). (*B*) pH distribution in the XZ plane of the microdroplet based on line profiles. (*C*) The variation of average pH, $[SO_4^{2-}]$, and $[HSO_4^-]$ in horizontal (X and Y) or vertical (Z) direction based on the coordinate in *B*. Values in the horizontal and vertical directions are marked as hollow and solid scatter, respectively. (*D*) Schematic diagram of pH distribution difference between aerosol and cloud microdroplets, where an abnormal pH increase (marked green) occurs near the edge of larger microdroplets.

(green region) occurs near the edge of larger droplets. Lhee et al. likewise found that the concentration of charged dyes progressively increased from the center to the edge of 7 µm droplets, while a decrease of the concentration was observed close to the interface in the cases of 24 and 28 µm droplets (30). This phenomenon in larger microdroplets can be attributed to the migration of molecules from the adjacent inner region to the interface, which may be driven by the interfacial electric field (EF) (9).

Particle Size Dictating pH Variation within Condensed Phases. The Fig. 4A details the effect of droplet size on pH distribution as well as acidity change (ΔpH) of microdroplets. The results show pH variation inside typical aerosol microdroplets as a function of normalized distance to the center. Overall, the smaller the size of the droplet is, the lower its interfacial pH and the greater the degree and zone of pH variation are. For small microdroplets (d ≤ 3.2 µm), the pH decreases continuously from the center (0.11 to 0.37) to the edge (–0.35 to –0.78). Whereas, as the diameter increases, a "pH-stable zone" begins to appear in the central region of the microdroplet while the edges remain more acidic. The width of this pH-stable zone increases with increasing droplet size; in other words, the "acidification zone" (the zone with the big absolute value of ΔpH) decreases accordingly. For example, the width of the acidification zone for 134.6 µm microdroplets is 0.137 (normalized distance, ND), which is almost 6 times smaller than that of the 2.9-µm microdroplet (ND = ~0.8). Additionally, for small microdroplets (d ≤ 3.2 µm), they showed a monotonic trend of pH decreasing from center to edge. For bigger microdroplets (21.9 µm ≤ d ≤ 134.6 µm), they all presented a sharp pH decrease in the region close to the interface, while the "pH-stable zone" is not entirely similar. When the size is larger than 21.9 µm, the pH first slowly increased from the center to the inner region of the edge, then sharply decreased to the lowest pH at the edge. The highest pH is observed at the inner region of the edge. Based on the statistical H^+ distribution of five microdroplets of different sizes, we proposed a potential method to estimate the average pH at the interface of ambient aerosols (*SI Appendix*, Note S8 and Fig. S15).

As reported, ions are dragged to the interface from the bulk through the electrostatic interactions and accumulate in nearby inner layers (31). Therefore, the $[H^+]$ at the microdroplet edge could partially reflect the electric field strength. As shown in Fig. 4B, the average edge pH possesses a good linear relationship with $\Delta[H^+]$, demonstrating the possible influence of average $[H^+]$ at the microdroplet edge on the pH gradient within the microdroplet. Moreover, the distribution of simulated EF (*SI Appendix*, Fig. S16) in microdroplets is consistent with that of species (32). The EF gradients are much larger at the edge of big microdroplets than that of small microdroplets (Fig. 4C). It implies that this pH gradient may be caused by the electrostatic interaction force from the interfacial electric field. This force migrates H^+ from the inside of microdroplets to its edge. Then, sulfates are protonated with H^+ leading to the enrichment of bisulfates. Fig. 4D shows the relationship between interfacial affinities of (bi)sulfate and microdroplet size. Obviously, SO_4^{2-} preferentially resides deeper in the interfacial region relative to HSO_4^-, and only HSO_4^- was detected in the microdroplet edge, consistent with the reported results (33). The normalized width layer containing only HSO_4^- (green columns) decreases from 0.12 to 0.02 when the microdroplet diameter increases from 2.5 to 33.9 µm, then remains stable (~0.01) within the bigger microdroplet. The surface preference of HSO_4^- becomes more obvious in small droplets, following the abovementioned lower pH and enhanced electric field at the surface of small microdroplets (detailed in *SI Appendix*, Note S9).

As illustrated in Fig. 4E, the $\Delta[H^+]$ is proportional to S/V with a surprising R^2 of 0.94. Meanwhile, the width (ΔL) of the acidification zone has a linear relationship with the logarithm of S/V. Accordingly, the pH distribution inside microdroplets can be estimated by S/V, which is favorable for improving the accuracy of the aerosol model prediction. In addition, we also investigated the pH distribution under low relative humidity (RH) of 35%. Compared to microdroplets under 90% RH (Fig. 3A), the pH gradient within the microdroplet under 35% RH was still present but less pronounced (*SI Appendix*, Fig. S17), especially in the one with a diameter of 9.0 µm. For instance, at 35% RH, the $[H^+]_{edge}$/$[H^+]_{center}$ of microdroplets with diameters of 9.0 and 24.4 µm is 2.26 and 1.64, respectively, while under 90% RH with a similar diameter, this ratio can reach 3.78 (9.1 µm-microdroplet) and 2.02 (27.0 µm-microdroplet) (Fig. 4A), respectively. The increased viscosity in the concentrated aerosol may inhibit ion migration and electric field formation (34, 35), resulting in a weaker pH gradient. For big microdroplets with radii of 23.6 and 38.2 µm, they are more prone to crystallize in the center of the microdroplet, leading to phase separation. The residual liquid phase of the microdroplet aerosol still exhibits a pH gradient and possesses a more acidic interface.

Discussion

As well known, pH plays a key role in the formation of secondary aerosol and inorganic salts (6, 17). Especially with the advances in single aerosol measurements, there is an increasing awareness of the importance of aerosol chemical mixing states (36). Up to now, the acid–base properties of aerosol microdroplet surface is an issue that remains incompletely elucidated and has raised intense controversies. Depending on the employed experimental method and theoretical technique, apparent opposite conclusions have been deduced for the interface affinity and spatial distribution of H_3O^+ and OH^- in macroscopic measurements (7). The preponderance of evidence in molecular-scale measurements supports the stronger surface propensity for protons (31, 33, 37). Recently, concentration gradient within microdroplets has been supported by studies of MD and laboratory (21, 29, 38, 39). As reported, water is more extensively self-ionized at the surface than in the bulk, and interfacial H_3O^+ exists as a stronger acid (a "super-acid") than their bulk counterparts (40). Because H_3O^+ could perturb the bulk hydrogen bonding network with three hydrogen bonds and is expelled to the surface, forming this special interface affinity of H_3O^+ (31).

Here, the pH imaging of microdroplets with a high resolution via a noncontact method suggests that there is not only a simple pH gradient inside the aerosol as previously reported (21), but also this pH distribution is complex and dependent on the aerosol size. For small aerosol microdroplets, their surface is more reactive due to a higher acidity, which largely changes our perception of the traditional chemical processes of aerosols. On the one hand, acid-catalyzed reactions within aerosols may be faster. For example, isoprene epoxydiols formation, peroxyhemiacetal formation, hydration, hemiacetal/acetal formation, and/or aldol condensation was enhanced in acidic condition (16). Thus, more acidic surfaces will promote the SOA formation and organic degradation. Low pH also reduced the light absorption of brown carbon (41), impacting the global climate. Besides, an acidic environment accelerates the dissolution of metals, such as iron and manganese, thereby accelerating photochemical reactions in the atmosphere, such as the oxidation of SO_2 and the Fenton reaction in aerosols (13–15). On the other hand, more acidic interfaces can affect the contribution of reaction pathways to species production. As reported, H^+ catalyzes the aqueous SO_2 oxidation pathways involving H_2O_2 and ROOH, offsetting the effects arising from the
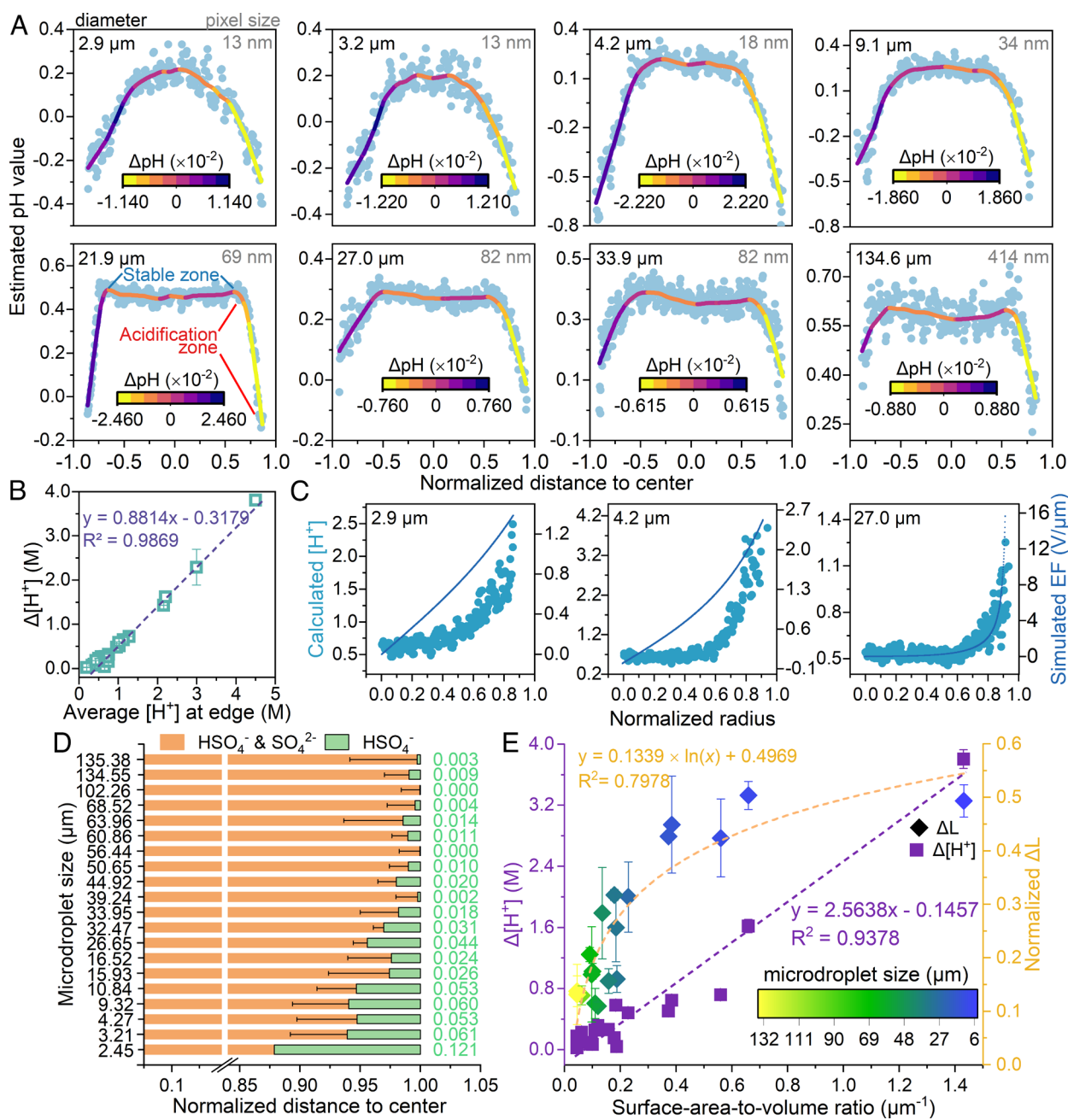
Fig. 4. The effect of particle size on stereoscopic pH distribution inside microdroplets. (*A*) The pH distribution within 8 microdroplets as a function of ND to the center where the starting and ending points of the microdroplet diameter in the X-direction (Fig. 2) are normalized to −1 and 1, respectively, and the microdroplet center is defined as ND = 0. Symbol color corresponds to ΔpH of microdroplet along X directions ($\Delta pH = pH_{x_{i+1}} - pH_{x_i}$). Microdroplet diameter and pixel size were marked as black and gray, respectively. (*B*) $\Delta[H^+]$ as a function of average $[H^+]$ at the microdroplet edge. (*C*) The distribution of calculated $[H^+]$ via pH and simulated EF based on reported model within microdroplets of different size. (*D*) The normalized width of the layer containing only HSO_4^- (green), and zone mixed of HSO_4^- and SO_4^{2-} (orange) within microdroplets of different diameters indicates the effect of microdroplet size on the surface preference of (bi)sulfate. (*E*) $\Delta[H^+]$ ($[H^+]_{edge} - [H^+]_{center}$) between the center and microdroplet edge as well as the width (ΔL) of the acidification zone as a function of normalized distance to the center. The $[H^+]_{edge}$ and $[H^+]_{center}$ were determined by the average of the pH values at the microdroplet edge.

pH-dependent solubility of SO_2 (42). $HONO_{(l)}$ will convert to $HONO_{(g)}$ under acidic conditions to thereby form hydroxyl radicals, increasing the oxidation of the atmosphere (43).

Our results also emphasize the importance of pH distributions in cloud drops and the size dependence of pH distributions. In general, semi-volatile species including NH_3, HNO_3, and low-molecular-weight organic acids typically exist in cloud drops as significant fractions. However, most species are likely to be more concentrated at more acidic interfaces, leading to different reaction processes compared with the bulk phase. Besides, the size dependence of pH distributions suggests that the smaller the aerosol, the more acidic its surface. The

diameter of the typical aerosol was defined to be less than 10 μm, even 50 to 1,000 nm (5, 17). As a result, the atmospheric process of aerosol, such as the uptake and oxidation of SO_x, will be influenced by the enriched bisulfate and more acidic pH at the aerosol surface. The spatial pH distribution in aerosol microdroplets reported here will facilitate a better understanding of atmospheric chemical processes. Besides, Wu et al. (33) reported that the aerosol liquid water plays a crucial role in haze formation over the North China Plain, while the results here suggested that the pH gradient may be strengthened with increased RH. It implied that the interfacial acidification of aerosol may have a significant impact on this process.

https://doi.org/10.1073/pnas.2219588120

Collectively, our study delineates the size-dependent pH gradient within aerosol microdroplets via SRS. Imaging microdroplets' pH with a high spatial resolution is realized. We found that the pH at the droplet edge is much more acidic than that at the centroid, with a 3.4-fold increase in [H^+] when the droplet size is 2.9 μm. This pH gradient is well supported by MD simulations. We also report a nonmonotonic pH variation from the center to the interface inside big microdroplets. Smaller microdroplets possess more acidic surface and internal concentration gradients, which can be quantitatively evaluated by S/V. These results shed light on the chemistry of aerosols where surface acidity has been linked to important atmospheric processes such as the uptake and oxidation of trace gases, acid-catalyzed degradation of organics, and formation of additional condensed phases. Our work adds to the current understanding of pH gradients in aerosol microdroplets and creates opportunities for further studies.

Materials and Methods

MRS Measurement. Like our previous work (44), the MRS of bulk solutions and aerosols in a quartz cell (*SI Appendix*, Fig. S1*A*) was recorded by XploRA Plus confocal spectrometer (Jobin Yvon, Horiba Gr, France) with 100× Olympus microscope objective (LMPLFLN100×, Olympus, N.A. = 0.8). The power of the external-cavity continuous-wave diode laser (532 nm) was set to 45 mW (50% of the maximum power) to improve the signal-to-noise ratio. Before the measurement, the instrument was calibrated against the Stokes Raman signal of pure Si [a silicon wafer ([110] crystal plane)] at 520 cm^{-1}. Every spectral resolution was 1 cm^{-1} over the range of 300 to 4,500 cm^{-1} with an acquisition time of 10 s and three accumulations. To obtain the 2D SO_4^{2-}/HSO_4^- and pH distribution of microdroplets, Raman mapping was conducted based on a motorized scanning table with a minimum step size of 0.2 μm. Each pixel represents a single Raman spectrum collected with the same setup as a bulk solution.

SRS Measurement. Our chemical imaging of SO_4^{2-}, HSO_4^-, and H_2O was based on a conventional SRS microscope as detailed in our previous work (22, 45). In brief, a commercial femtosecond laser system (Insight DS+, Spectra-Physics) produced two synchronized pulse trains at 80MHz. The fixed fundamental output of 1,040 nm was employed as the Stokes beam, while the tunable optical parametric oscillator output (680 to 1,300 nm) served as the pump beam. To acquire high spectral resolution (~13 cm^{-1}), pulse durations of the pump and Stokes beams were chirped and stretched to several picoseconds by passing through SF57 glass rods. The intensity of the 1,040 nm Stokes beam was modulated at 1/4 of the laser pulse repetition rate using an electro-optical modulator (EOM, EO-AM-R-20-C2, Thorlabs). The two laser beams were spatially and temporally overlapped via a dichroic mirror, then delivered into a laser scanning microscope (FV1200, Olympus) equipped with galvo mirrors for raster scanning. The combined beams were focused onto the microdroplet by a 60× water immersion objective lens (Olympus, UPLSAPO 60XWIR, NA 1.2). The stimulated Raman loss signal was optically filtered (CARS ET890/220, Chroma), detected by a homemade back-biased photodiode (PD), and demodulated with a lock-in amplifier (HF2LI, Zurich Instruments) to feed the analog input of the microscope to form images with the size of 512 × 512 pixels. The microdroplet was kept in a closed homemade chamber to ensure stable chemical imaging. The laser powers of 20 mW for the pump and 30 mW for Stokes pulses were used for samples. A lock-in time constant was set as 2 to 10 μs to match the pixel dwell time. All images were taken in transmission mode. The Raman bands included the $\nu_s(SO_4^{2-})$ and the $\nu_s(HSO_4^-)$ which were recorded at the pump laser wavelength of 940 nm, while the signal of $\nu(H_2O)$ was measured with the tuned 776 nm pump beam. The optical layout is illustrated in *SI Appendix*, Fig. S1*B*.

Construction and Verification of SO_4^{2-}/HSO_4^- Calibration Curves. According to the IS method, standard solutions of Na_2SO_4 and $NaHSO_4$ within the widest possible range of concentrations are used to create calibration curves relating [SO_4^{2-}] and [HSO_4^-] to the SRS intensity ratio of the $\nu_s(SO_4^{2-})$/$\nu(H_2O)$

and $\nu_s(HSO_4^-)$/$\nu(H_2O)$. The calibration curve of [SO_4^{2-}] is established first by a series of Na_2SO_4 solutions (Fig. 1*B*). After that, the sulfate calibration curve is used to calculate [HSO_4^-] in the SO_4^{2-}/HSO_4^- equilibrium of $NaHSO_4$ standard solutions through elemental conservation (Fig. 1*B*), obtaining the calibration curve of [HSO_4^-]. To verify the accuracy of SRS quantitative analysis, similar calibration curves relating [SO_4^{2-}] and [HSO_4^-] to the MRS integrated peak area ratio of the $\nu_s(SO_4^{2-})$/$\nu(H_2O)$ and $\nu_s(HSO_4^-)$/$\nu(H_2O)$ were created first (*SI Appendix*, Fig. S3). Then, the MRS and SRS spectra (*SI Appendix*, Fig. S4) of a series of mixed solutions (Fig. 1*E*) with preknown total [S] were employed to compare the accuracy of two calibration curves: integrated MRS peak area ratio versus concentration (*SI Appendix*, Fig. S3*C*) and SRS peak intensity ratio versus concentration (Fig. 1*D*). All chemicals are purchased from Sigma-Aldrich (Shanghai) Trading Co. Ltd. with high purity (>99%), and the solution pH is detected by a probe (S210, Mettler Toledo).

Generation and Collection of Aerosol Droplets. Microdroplets are generated from the mixed solution of 300 mM $NaHSO_4$ and 50 mM Na_2SO_4 via a homemade atomizer of 100 mL at room temperature and naturally dispersed on superhydrophobic coverslips. Then, that hydrophobic coverslip with microdroplets is quickly flipped over onto the central perforated slides, forming a closed chamber with the help of another original coverslip and a sealant, as shown in *SI Appendix*, Fig. S8. Before being probed by SRS or MRS, the chamber was held for 5 min at room condition (23 °C, 101.325 kPa) to ensure that the droplets became stable. The RH in the chamber is 90 ± 2.5%. The pictured micrometer-sized droplets indicated a successful microdroplet collection. Owing to the limitation of the analyzer (SRS/MRS), we prepared the superhydrophobic coverslips as reported in literature (46).

Data Processing in Image Plotting. For the distribution of pH, [SO_4^{2-}], and [HSO_4^-], all the images of species distribution were plotted based on corresponding SRS images and MATLAB software. In detail, the SRS image, including H_2O (3,420 cm^{-1}), SO_4^{2-} (985 cm^{-1}), and HSO_4^- (1,050 cm^{-1}), in Tag Image File Format, is imported into MATLAB software as a 2D matrix. Consequently, using the cells in the matrix as calculation units, the [SO_4^{2-}] and [HSO_4^-] in any cells can be calculated from the corresponding calibration curves based on SRS. Finally, the figure of (bi)sulfates distribution can be obtained by converting their two-dimensional matrices into images again. Furthermore, the matrices of calculated [SO_4^{2-}] and [HSO_4^-] were used to produce the matrix of pH based on Fig. 1*D* and Eqs. **1A** and **1B**, as well as the image of pH distribution. For the line profile, all the images of species distribution were plotted based on the corresponding SRS images and the software of Image J. In detail, the SRS images of H_2O, SO_4^{2-}, and HSO_4^- were merged into one image by Image J software. Then, the Image J was used to read data of the SRS image in a certain direction. As a result, we obtained line profiles of H_2O, SO_4^{2-}, and HSO_4^- in one direction, that derived from the same position of the microdroplet (*SI Appendix*, Fig. S13). After that, the [SO_4^{2-}], [HSO_4^-], and pH can be determined through calibration curves in Fig. 1*D* and Eqs. **1A** and **1B**.

Computational Details. To obtain thermodynamic properties and species distribution within microdroplets, a classical MD calculation was performed for sulfate microdroplet systems. An aerosol microdroplet of Na_2SO_4 and $NaHSO_4$ was constructed in this work. The radius of the aerosol microdroplet is 5 nm, and a 12 × 12 × 12 nm^3 simulation box which contains H_3O^+, Na^+, HSO_4^-, SO_4^{2-}, and H_2O molecules was used. According to our experimental results, [HSO_4^-] and [SO_4^{2-}] were set at 3.8 and 2.3 M, respectively. The concentration of free H_3O^+ (activity of the H^+ ion) was determined by our empirical formula (Eqs. **1A** and **1B**) to be 1.047 M. Then, the [Na^+] was determined at 7.353 M based on the conservation of charge. Accordingly, the [H_2O] was calculated at ~36.44 M (29). Periodic boundary conditions were applied in all the three directions (47). The ions were parameterized with the program acpype.py using Antechamber and the GAFF forcefield (48–50). This GAFF forcefield has been widely used for small molecules in atmospheric processes (51, 52). Water molecules were simulated using the transferable intermolecular potential with the three points (TIP3P) model (50). A cutoff distance of 12.0 Å was used for Lennard–Jones and real space coulombic interactions. The Particle Mesh Ewald method was also employed with an interpolation order of 6 with 1.0 Å grid spacing (53). Before the MD began, energy minimizations were carried out. Then, the systems were equilibrated for 200 ps at the temperature of 298 K

(NVT). After equilibration, the simulated systems were run for 50 ns in an NVT ensemble at 298 K. The timestep was 1 fs, and the trajectories were collected every 1 ps. The MD trajectories resulting from the dynamic simulations were processed to extract the structural and dynamical properties of the simulated systems. To identify the distribution of ions, the number of ions per 0.5 Å from the center to the air–water interface and the X–Y planar density maps (cross-section of the aerosol microdroplet between 5.5 and 6.5 nm along z-coordinate) was calculated. All the MD calculations were executed by the software package of GROMACS 2019.6. And MD configurations were visualized by the VMD package (54).

Data, Materials, and Software Availability. All study data are included in the article and/or supporting information.

Author affiliations: aShanghai Key Laboratory of Atmospheric Particle Pollution and Prevention, Department of Environmental Science & Engineering, Fudan University, Shanghai 200433, Peoples' Republic of China; bNational Observations and Research Station for Wetland Ecosystems of the Yangtze Estuary, Fudan University, Shanghai 200433, People's Republic of China; cIntegrated Research on Disaster Risk, and RDR International Center of Excellence on Risk Interconnectivity and Governance on Weather, Fudan University, Shanghai 200433, People's Republic of China; dShanghai Institute of Pollution Control and Ecological Security, Shanghai 200092, People's Republic of China; eState Key Laboratory of Surface Physics and Department of Physics, Fudan University, Shanghai 200433, Peoples' Republic of China; fAcademy for Engineering and Technology, Fudan University, Shanghai 200433, Peoples' Republic of China; gDepartment of Atmospheric and Oceanic Sciences, Fudan University, Shanghai 200433, Peoples' Republic of China; hKey Laboratory of Cluster Science, Ministry of Education of China, School of Chemistry and Chemical Engineering, Beijing Institute of Technology, Beijing 100081, Peoples' Republic of China; iDepartment of Civil and Environmental Engineering, University of Wisconsin-Madison, Madison, WI 53706; jUniversité de Lyon, Université Claude Bernard Lyon 1, CNRS, IRCELYON, Villeurbanne 69626, France; kInstitut de Combustion, Réactivité et Environnement (ICARE), Centre National de la Recherche Scientifique/The Observatory of Sciences of the Universe in the Center (CNRS/OSUC), Orléans Cedex 2, 45071, France; lMohammed VI Polytechnic University, Lot 660, Hay Moulay Rachid, 43150 Benguerir, Morocco; mLeibniz Institute for Tropospheric Research, Atmospheric Chemistry Department, Leipzig 04318, Germany; nDepartment of Earth and Environmental, Sciences, University of Pennsylvania, Philadelphia, PA 19104; and oDepartment of Chemistry, University of Pennsylvania, Philadelphia, PA 19104

Author contributions: M.J., L.Z., and J.S.F. designed research; K.G., and J.A. performed research; L.L. K.G., contributed new reagents/analytic tools; K.G., J.A., K.L., Y.L., G.X., T.W., Z.W., X.Z., L.Z., and J.S.F. analyzed data; K.L., L.L., Y.L., G.X., T.W., and H.C. visualization; H.W. and C.G. review & editing; A.M., H.H., L.W., and J.C. review and editing; and K.G., J.A., H.C., H.W., C.G., A.M., H.H., L.W., L.Z., J.C., and M.J. wrote the paper.

1. C. R. Ruehl, J. F. Davies, K. R. Wilson, An interfacial mechanism for cloud droplet formation on organic aerosols. *Science* **351**, 1447–1450 (2016).
2. D. C. Clary, CHEMISTRY., Quantum dynamics in the smallest water droplet. *Science* **351**, 1267–1268 (2016).
3. J. K. Lee *et al.*, Condensing water vapor to droplets generates hydrogen peroxide. *Proc. Natl. Acad. Sci. U.S.A.* **117**, 30934–30941 (2020).
4. G. Zheng *et al.*, Multiphase buffer theory explains contrasts in atmospheric aerosol acidity. *Science* **369**, 1374–1377 (2020).
5. R. C. Sullivan, H. Boyer-Chelmo, K. Gorkowski, H. Beydoun, Aerosol optical tweezers elucidate the chemistry, acidity, phase separations, and morphology of atmospheric microdroplets. *Acc. Chem. Res.* **53**, 2498–2509 (2020).
6. M. Jang, N. M. Czoschke, S. Lee, R. M. Kamens, Heterogeneous atmospheric aerosol production by acid-catalyzed particle-phase reactions. *Science* **298**, 814–817 (2002).
7. M. F. Ruiz-Lopez, J. S. Francisco, M. T. C. Martins-Costa, J. M. Anglada, Molecular reactions at aqueous interfaces. *Nat. Rev. Chem.* **4**, 459–475 (2020).
8. I. Nam, J. K. Lee, H. G. Nam, R. N. Zare, Abiotic production of sugar phosphates and uridine ribonucleoside in aqueous microdroplets. *Proc. Natl. Acad. Sci. U.S.A.* **114**, 12396–12400 (2017).
9. H. Xiong, J. K. Lee, R. N. Zare, W. Min, Strong electric field observed at the interface of aqueous microdroplets. *J. Phys. Chem. Lett.* **11**, 7423–7428 (2020).
10. X. Yan, R. M. Bain, R. G. Cooks, Organic reactions in microdroplets: Reaction acceleration revealed by Mass Spectrometry. *Angew. Chem. Int. Ed.* **55**, 12960–12972 (2016).
11. Z. Wei, Y. Li, R. G. Cooks, X. Yan, Accelerated reaction kinetics in microdroplets: Overview and recent developments. *Annu. Rev. Phys. Chem.* **71**, 31–51 (2020).
12. K.-H. Huang, Z. Wei, R. G. Cooks, Accelerated reactions of amines with carbon dioxide driven by superacid at the microdroplet interface. *Chem. Sci.* **12**, 2242–2250 (2021).
13. W. Wang *et al.*, Sulfate formation is dominated by manganese-catalyzed oxidation of SO2 on aerosol surfaces during haze events. *Nat. Commun.* **12**, 1993 (2021).
14. T. Liu, J. P. D. Abbatt, Oxidation of sulfur dioxide by nitrogen dioxide accelerated at the interface of deliquesced aerosol particles. *Nat. Chem.* **13**, 1173–1177 (2021).
15. X. Kong *et al.*, A surface-promoted redox reaction occurs spontaneously on solvating inorganic aerosol surfaces. *Science* **374**, 747–752 (2021).
16. H. O. T. Pye *et al.*, The acidity of atmospheric particles and clouds. *Atmos. Chem. Phys.* **20**, 4809–4888 (2020).
17. A. P. Ault, Aerosol acidity: Novel measurements and implications for atmospheric chemistry. *Acc. Chem. Res.* **53**, 1703–1714 (2020).
18. K. J. Angle *et al.*, Acidity across the interface from the ocean surface to sea spray aerosol. *Proc. Natl. Acad. Sci. U.S.A.* **118**, e2018397118 (2021).
19. M. Li *et al.*, Aerosol pH and ion activities of HSO$_4^-$ and SO$_4^{2-}$ in supersaturated single droplets. *Environ. Sci. Technol.* **56**, 12863–12872 (2022).
20. L. F. Li, Z. Chen, P. Liu, Y. H. Zhang, Direct measurement of pH evolution in aerosol microdroplets undergoing ammonium depletion: A surface-enhanced Raman spectroscopy approach. *Environ. Sci. Technol.* **56**, 6274–6281 (2022).
21. H. Wei *et al.*, Aerosol microdroplets exhibit a stable pH gradient. *Proc. Natl. Acad. Sci. U.S.A.* **115**, 7272–7277 (2018).
22. J. Ao *et al.*, Rapid, 3D chemical profiling of individual atmospheric aerosols with stimulated Raman scattering microscopy. *Small Methods* **4**, 1900600 (2019).
23. D. Fu *et al.*, Imaging the intracellular distribution of tyrosine kinase inhibitors in living cells with quantitative hyperspectral stimulated Raman scattering. *Nat. Chem.* **6**, 614–622 (2014).
24. M. C. Wang, W. Min, C. W. Freudiger, G. Ruvkun, X. S. Xie, RNAi screening for fat regulatory genes with SRS microscopy. *Nat. Methods* **8**, 135–138 (2011).
25. M. J. Pelletier, Quantitative analysis using Raman spectrometry. *Appl. Spectrosc.* **57**, 20A–42A (2016).
26. P. J. Aarnoutse, J. A. Westerhuis, Quantitative Raman reaction monitoring using the solvent as internal standard. *Anal. Chem.* **77**, 1228–1236 (2005).
27. R. Buck *et al.*, Measurement of pH. Definition, standards, and procedures (IUPAC Recommendations 2002). *Pure Appl. Chem.* **74**, 2169–2200 (2002).
28. D. C. Harris, *Quantitative Chemical Analysis* (Macmillan, 2010).
29. W. Zhang *et al.*, Mechanism for rapid conversion of amines to ammonium salts at the air-particle interface. *J. Am. Chem. Soc.* **143**, 1171–1178 (2021).
30. S. Lhee *et al.*, Spatial localization of charged molecules by salt ions in oil-confined water microdroplets. *Sci. Adv.* **6**, eaba0181 (2020).
31. P. B. Petersen, R. J. Saykally, On the nature of ions at the liquid water surface. *Annu. Rev. Phys. Chem.* **57**, 333–364 (2006).
32. C. F. Chamberlayne, R. N. Zare, Simple model for the electric field and spatial distribution of ions in a microdroplet. *J. Chem. Phys.* **152**, 184702 (2020).
33. W. Hua, D. Verreault, H. C. Allen, Relative order of sulfuric acid, bisulfate, hydronium, and cations at the air-water interface. *J. Am. Chem. Soc.* **137**, 13920–13926 (2015).
34. Z. Lei *et al.*, Initial state-dependent aerosol phase state and morphology after uptake of isoprene epoxydiols (IEPOX). *Environ. Sci. Technol.* **56**, 10596–10607 (2022).
35. R. Schmedding *et al.*, Predicting secondary organic aerosol phase state and viscosity and its effect on multiphase chemistry in a regional-scale air quality model. *Atmos. Chem. Phys.* **20**, 8201–8225 (2020).
36. A. P. Ault, J. L. Axson, Atmospheric aerosol chemistry: Spectroscopic and microscopic advances. *Anal. Chem.* **89**, 430–452 (2017).
37. N. Agmon *et al.*, Protons and hydroxide ions in aqueous systems. *Chem. Rev.* **116**, 7642–7672 (2016).
38. H. Hao, I. Leven, T. Head-Gordon, Can electric fields drive chemistry for an aqueous microdroplet? *Nat. Commun.* **13**, 280 (2022).
39. H. Xiong, J. K. Lee, R. N. Zare, W. Min, Strong concentration enhancement of molecules at the interface of aqueous microdroplets. *J. Phys. Chem. B* **124**, 9938–9944 (2020).
40. Y. Tabe, N. Kikkawa, H. Takahashi, A. Morita, Surface acidity of water probed by free energy calculation for trimethylamine protonation. *J. Phys. Chem. C* **118**, 977–988 (2013).
41. S. M. Phillips, A. D. Bellcross, G. D. Smith, Light absorption by brown carbon in the southeastern united states is pH-dependent. *Environ. Sci. Technol.* **51**, 6782–6790 (2017).
42. T. Liu, A. W. H. Chan, J. P. D. Abbatt, Multiphase oxidation of sulfur dioxide in aerosol particles: Implications for sulfate formation in polluted environments. *Environ. Sci. Technol.* **55**, 4227–4242 (2021).
43. D. Xia *et al.*, Heterogeneous formation of HONO catalyzed by CO₂. *Environ. Sci. Technol.* **55**, 12215–12222 (2021).
44. K. Gong *et al.*, Sensing pH of individual microdroplet by combining SERS and indicator paper. *Sens. Actuators B Chem.* **346**, 130521 (2021).
45. J. Ao *et al.*, Switchable stimulated Raman scattering microscopy with photochromic vibrational probes. *Nat. Commun.* **12**, 3089 (2021).
46. J. K. Lee *et al.*, Spontaneous generation of hydrogen peroxide from aqueous microdroplets. *Proc. Natl. Acad. Sci. U.S.A.* **116**, 19294–19298 (2019).
47. N. Sukumar, J. E. Pask, Classical and enriched finite element formulations for Bloch-periodic boundary conditions. *Int. J. Numer. Meth. Eng.* **77**, 1121–1138 (2009).
48. B. Q. Wei, L. H. Weaver, A. M. Ferrari, B. W. Matthews, B. K. Shoichet, Testing a flexible-receptor docking algorithm in a model binding site. *J. Mol. Biol.* **337**, 1161–1182 (2004).
49. J. Wang, R. M. Wolf, J. W. Caldwell, P. A. Kollman, D. A. Case, Development and testing of a general amber force field. *J. Comput. Chem.* **25**, 1157–1174 (2004).
50. W. L. Jorgensen, J. Chandrasekhar, J. D. Madura, R. W. Impey, M. L. Klein, Comparison of simple potential functions for simulating liquid water. *J. Chem. Phys.* **79**, 926–935 (1983).
51. D. J. Bustos, B. Temelso, G. C. Shields, Hydration of the sulfuric acid-methylamine complex and implications for aerosol formation. *J. Phys. Chem. A* **118**, 7430–7441 (2014).
52. J. Liu *et al.*, Mechanism of the gaseous hydrolysis reaction of SO₂: Effects of NH₃ versus H₂O. *J. Phys. Chem. A* **119**, 102–111 (2015).
53. U. Essmann *et al.*, A smooth particle mesh ewald method. *J. Chem. Phys.* **103**, 8577–8593 (1995).
54. W. Humphrey, A. Dalke, K. Schulten, VMD: Visual molecular dynamics. *J. Mol. Graph.* **14**, 27–38 (1996).